

# A Radiometrically Dated Record of Antarctic Ice Sheet Response to Millennial-Scale Climate Cycles during Glacials and Interglacials

Gavin Piccione (✉ [gpiccion@ucsc.edu](mailto:gpiccion@ucsc.edu))

University of California Santa Cruz <https://orcid.org/0000-0002-7637-9796>

Terrence Blackburn

Santa Cruz

Slawek Tulaczyk

University of California, Santa Cruz <https://orcid.org/0000-0002-9711-4332>

Troy Rasbury

Stony Brook University <https://orcid.org/0000-0003-0591-4461>

Mathis Hain

University of California, Santa Cruz <https://orcid.org/0000-0002-8478-1857>

Daniel Ibarra

Brown University <https://orcid.org/0000-0002-9980-4599>

Katharina Methner

Senckenberg <https://orcid.org/0000-0002-3753-8256>

Chloe Tinglof

University of California Santa Cruz

Brandon Cheney

University of California Santa Cruz

Paul Northrup

Kathy Licht

Indiana University-Purdue University

---

## Article

### Keywords:

**Posted Date:** February 11th, 2022

**DOI:** <https://doi.org/10.21203/rs.3.rs-1300507/v1>

**License:**   This work is licensed under a Creative Commons Attribution 4.0 International License.

[Read Full License](#)

---

**Version of Record:** A version of this preprint was published at Nature Communications on September 15th, 2022. See the published version at <https://doi.org/10.1038/s41467-022-33009-1>.

# **A Radiometrically Dated Record of Antarctic Ice Sheet Response to Millennial-Scale Climate Cycles during Glacials and Interglacials**

**Authors:** G. Piccione<sup>1\*</sup>, T. Blackburn<sup>1</sup>, S. Tulaczyk<sup>1</sup>, E.T. Rasbury<sup>2</sup>, M. Hain<sup>1</sup>, D.E. Ibarra<sup>3,4</sup>, K. Methner<sup>3</sup>, C. Tinglof<sup>1</sup>, B. Cheney<sup>1</sup>, P. Northrup<sup>2</sup>, K. Licht<sup>6</sup>

<sup>1</sup>Earth and Planetary Sciences, University of California Santa Cruz, Santa Cruz, CA 95064, USA

<sup>2</sup>Department of Geosciences, Stony Brook University, Stony Brook, NY 11794, USA.

<sup>3</sup>Department of Earth and Planetary Science, University of California Berkeley, CA 94720 USA

<sup>4</sup>Department of Earth, Environmental and Planetary Science, and the Institute at Brown for Environment and Society, Brown University, Providence, RI 02912, USA

<sup>5</sup>Department of Geological Sciences, Stanford University, Stanford, CA 94305, USA

<sup>6</sup>Department of Earth Sciences, Indiana University-Purdue University Indianapolis, IN 46202, USA

\*Correspondence to: [gpiccion@ucsc.edu](mailto:gpiccion@ucsc.edu)

**Records of changing ice mass in offshore sediments and ice cores suggest that the West Antarctic ice sheet experienced millennial-scale ice loss during the last termination. However, the distal location and short temporal coverage of these records leads to uncertainty in both the spatial footprint of ice response, and whether this response persists outside of glacial terminations. Here we present a >100kyr archive of episodic Antarctic ice sheet basal melt events recorded by mineralogic variation in subglacial precipitates. <sup>234</sup>U-<sup>230</sup>Th dates for two precipitates are used to build a time series of 32 opal-calcite transitions that correspond to Late Pleistocene millennial-scale climate cycles, with precipitation of opal during cold periods and calcite during warm periods. Geochemical data indicate that opal precipitation occurs via cryoconcentration of silica in brines beneath the ice sheet margin, while calcite precipitation is triggered by the addition of subglacial meltwater originating from the ice sheet interior. These freeze-flush cycles represent changes in subglacial hydrologic-connectivity driven by ice sheet velocity fluctuations, which likely occur in response to Southern Ocean thermal forcing acting on grounding lines within the Ross Embayment. Our results suggest that oscillating temperatures in the Southern Ocean affect the mass of the Antarctic ice sheet by regulating the delivery of heat to buttressing ice shelves and grounding lines on millennial timescales, regardless of the background climate state.**

---

One of the persistent challenges involved in both reconstructions and projections of future global mean sea level is determining what sectors of the Antarctic Ice Sheet (AIS) are vulnerable to significant retreat, the timescales of such retreat, and the conditions that trigger retreat<sup>1</sup>. Modern observations<sup>2-4</sup> of ice loss near marine-terminating ice sheet margins demonstrate the potential for rapid AIS mass fluctuations brought on by changing Southern Ocean (SO) temperature<sup>5</sup> (hereafter referred to as ocean thermal forcing). The key link between this ocean thermal forcing and ice sheet mass lies in the delivery of heat to the marine-terminating ice sheet margins, affecting ice shelves and grounding lines. Ice sheet stability is regulated by ice shelves<sup>6,7</sup> and grounding line positions<sup>8</sup>, which are vulnerable to thinning and retreat when contacted by warm ocean waters. Ice sheet models suggest that ice shelf decay can result in enhanced flow of grounded

45 ice up to 1000 km upstream of the grounding lines of large and fast outlet glaciers and ice streams<sup>9</sup>. On  
46 millennial timescales this feedback can cause substantial velocity changes in these fast-flowing ice drainage  
47 pathways<sup>10</sup>, ultimately affecting continent-wide ice sheet mass balance<sup>11</sup>.

48 Such millennial-scale SO temperature oscillations are driven by a feedback between ocean-  
49 atmosphere-cryosphere teleconnections that is modulated by Atlantic Meridional Overturn Circulation  
50 (AMOC)<sup>12</sup>: the mean state ocean circulation responsible for cross-equatorial heat transport from the  
51 Southern Hemisphere to the Northern Hemisphere (SH and NH). Changes to the intensity of AMOC result  
52 in out-of-phase polar temperature cycles<sup>13</sup> recorded by isotopic climate proxies in ice cores, identified as  
53 Dansgaard-Oeschger cycles in the Greenland ice core records and Antarctic Isotope Maxima (AIM) events  
54 in Antarctic ice core records. For example, during times of decreased AMOC or slow northerly transport  
55 of heat, the SH temperature increases at the expense of the NH, which is manifested as an increase in the  
56  $\delta^{18}\text{O}$  composition in Antarctic ice cores and a decrease in  $\delta^{18}\text{O}$  composition in Greenland ice cores (e.g., 48  
57 to 47ka in figure 1f, g). As AMOC recovers the NH temperature warms rapidly on decadal timescales while  
58 the SH gradually cools (e.g., at 46.7ka in figure 1f, g). This oceanic teleconnection, called the bipolar  
59 seesaw, also affects atmospheric circulation by regulating the temperature gradient between the middle and  
60 high latitudes<sup>14</sup>, which shifts the intertropical convergence zone (ITCZ) north during SH cold periods and  
61 south during SH warm periods. As the ITCZ migrates southwards during AIM events, SH westerly winds  
62 experience parallel meridional shifts and strengthening<sup>15</sup>, causing upwelling of relatively warm circumpolar  
63 deep waters (CDW) onto the Antarctic continental shelf<sup>16</sup>. Consequently, reconstructions of Pleistocene SO  
64 temperatures<sup>17</sup> demonstrate millennial warm-cold cycles in sea surface temperatures (SST) that are in-phase  
65 with ice core records of SH climate. Antarctic marginal ice is affected by these upwelling cycles, which  
66 deliver CDW to the base of ice shelves and grounding lines, triggering enhanced basal melting and retreat  
67 during SH millennial warm periods<sup>5</sup>.

68 Although ice sheet models<sup>10,18</sup> and modern observations<sup>2-4</sup> indicate that the AIS is susceptible to  
69 ice loss through ocean thermal forcing, regional differences in ice bed topography, drainage geometry, and  
70 ice thickness<sup>19</sup> in peripheral sectors of Antarctica may lead to geographic differences in grounding line  
71 vulnerability, adding spatiotemporal complexity to ice sheet response. Millennial-scale SO upwelling also  
72 varies in intensity depending on the background climate state, with the slowest AMOC causing increased  
73 SO upwelling during glacial terminations, and relatively strong AMOC resulting in weaker SO upwelling  
74 during interglacial periods<sup>20,21</sup>. Therefore, geologic evidence of AIS evolution across a wide geographic  
75 range and diverse climate states is necessary to ground truth simulations of suborbital changes in ice mass.  
76 However, existing geologic records documenting millennial-scale AIS mass loss<sup>22-24</sup> are limited to bipolar  
77 seesaw events during the last two glacial terminations, are constrained by low-resolution age models, and  
78 are restricted spatially to ice shelf systems and offshore sediments. This leaves the regional extent and  
79 magnitude of AIS response to suborbital climate change unconstrained. Here, we present observations from  
80 an archive of subglacial hydrologic evolution recorded by chemical precipitates that formed >900km apart  
81 beneath the EAIS over a combined >100kyr period during the Pleistocene. This dataset provides a novel  
82 sequence of high-resolution U-series age constraints on ice sheet evolution in response to millennial-scale  
83 climate change. Mineralogic and geochemical variations in subglacial precipitates provide evidence for  
84 basal hydrologic changes that are correlated with bipolar seesaw-related SH climate cycles. Combining  
85 precipitate data with a reduced-complexity model of ice sheet thermodynamics, we demonstrate a link  
86 between subglacial hydrologic conditions and millennial-scale changes in ice sheet velocity.

87

## 88 RESULTS

### 89 Changes in Subglacial Precipitate Mineralogy Correlated with Millennial Climate Cycles

90 In this study, we report geochronological and geochemical results collected from two subglacial  
91 precipitates: PRR50489, which formed in the David Glacier catchment and was collected at Elephant  
92 Moraine; and MA113, which formed beneath ice feeding Law Glacier and was collected at Mount Achernar  
93 moraine (Fig. 2). These samples were precipitated over tens of thousands of years in subglacial aqueous  
94 systems on the EAIS side of the Transantarctic Mountains (TAM), and were subsequently eroded and  
95 transported in exhumed sections of basal ice to be finally deposited on the surface within supraglacial

96 moraines<sup>25</sup>. PRR50489 and MA113 are 3 and 9cm thick respectively, with alternating layers of calcite and  
97 opal (Extended Data Fig. 1) implying cyclic change in the subglacial environment.

98 We measured <sup>234</sup>U-<sup>230</sup>Th ages on eleven opal layers from PRR50489 that constrain the timeframe  
99 of precipitation from 230 to 147ka (Fig. 1i), and ten opal and calcite layers from MA113 ranging in age  
100 from 55 to 42ka (Fig. 1f). We construct a stratigraphic age model for each sample using a Bayesian Markov  
101 chain Monte Carlo model in which the principal of superposition is imposed on each dated layer to refine  
102 age estimates based on stratigraphic order<sup>26</sup> (Extended Data Fig. 2). Depth profiles of Si and Ca  
103 concentration collected using Energy Dispersive X-ray Spectroscopy provide a continuous representation  
104 of sample mineralogy: with high Ca areas representative of calcite and low Ca areas representative of opal.  
105 We pair stratigraphic age models with Ca concentration spectra to create timeseries describing the  
106 oscillations of precipitate mineralogy (Fig. 1a,d). These mineralogic timeseries reveal a temporal cyclicity  
107 in opal deposition, with opal layers in PRR50489 precipitated every 8-10kyr between marine isotope stages  
108 (MIS) 7 and 6, and opal layers in MA113 precipitated every 2-4kyr during MIS 3 (Fig. 1a, d). To investigate  
109 a possible link between cycles of precipitate mineralogy and climate, we compare mineralogic timeseries  
110 for each precipitate with climate proxies in both Antarctic<sup>27,28</sup> (Fig. 1b,e,f) and Greenland<sup>29</sup> (Fig. 1g) ice  
111 cores. Comparison between Ca-spectra and Antarctic temperature proxies reveals a highly regular linear  
112 relationship between climate cycles and precipitate mineralogy, with calcite formation (high Ca wt%)  
113 during warm AIM peaks, and opal formation (low Ca wt%) during Antarctic cold periods (Fig. 1). Moving  
114 window correlation calculations between MA113 and PRR50489 mineralogic spectra and SH climate  
115 proxies from Antarctic ice core records demonstrate a significant temporal correlation between the two  
116 records throughout the sampling period (Extended Data Fig. 3). This synchrony indicates that bipolar-  
117 seesaw-driven climate change trigger variability in EAIS basal environments.

### 118 119 **Millennial-Scale Cycles in Subglacial Hydrologic Connectivity**

120 To understand the link between ocean-atmosphere-cryosphere teleconnections and the mineralogic  
121 composition of subglacial precipitates, we first utilize geochemical and isotopic measurements to  
122 characterize the provenance of opal and calcite source fluids. The carbon and oxygen isotopic compositions  
123 ( $\delta^{18}\text{O}_{\text{VSMOW}}$ ) of opal and calcite forming waters are distinct for both PRR50489 (Fig. 3a) and MA113 (Fig.  
124 3b), with calcites forming from waters with extremely depleted  $\delta^{18}\text{O}$ , and opals forming from waters with  
125  $\delta^{18}\text{O}$  values up to 7‰ more enriched. The depleted  $\delta^{18}\text{O}$  compositions of the calcite endmember suggest  
126 origination of meltwaters generated beneath the EAIS interior<sup>30,31</sup>, as similarly depleted  $\delta^{18}\text{O}$  values are  
127 found only in ice from the high polar plateau<sup>32</sup>. The heaviest  $\delta^{18}\text{O}$  compositions of the opal endmember  
128 fluid (-46.15‰ for PRR50489 and -52.10‰ for MA113) are similar to the  $\delta^{18}\text{O}$  of ice proximal to the region  
129 where samples were exhumed<sup>31,33</sup>, suggesting that these waters originate as meltwater from marginal ice.  
130 Another distinguishing characteristic of opal and calcite forming waters are their cerium anomalies (Ce\*),  
131 a proxy for redox conditions<sup>34</sup> (Fig. 3; Extended Data Fig. 4c). In both samples, Ce\* correlates with sample  
132 mineralogy, with calcite Ce\* values indicating precipitation from oxidizing waters (Ce\*<1), while the most  
133 <sup>18</sup>O enriched opals exhibit Ce\* values indicating precipitation from reduced waters (Ce\*>1) (Fig. 3;  
134 Extended Data Fig. 4c). In most cases,  $\delta^{18}\text{O}$  values of opal scale with Ce\*, pointing to mixing between  
135 oxidized and reducing water during the formation of both minerals (Fig. 3a,b). Depleted  $\delta^{13}\text{C}$  compositions  
136 (-23‰ for PRR50489 and -18‰ for MA113) of calcite forming waters imply that their carbon is sourced  
137 from subglacial organic matter that is oxidized during microbial respiration, consistent with observations  
138 from other EAIS basal aqueous systems<sup>35</sup>.

139 Calcite layers in both precipitates exhibit trends in  $\delta^{13}\text{C}$  and  $\delta^{18}\text{O}$  compositional space that suggest  
140 mixing between two isotopically distinct fluids with different carbon concentrations (Fig 3). To match the  
141 trends in the calcite data for PRR50489 and MA113, the  $\delta^{13}\text{C}$  and  $\delta^{18}\text{O}$  depleted, endmember calcite forming  
142 water must have 40-fold and 5-fold higher of the total carbon concentration respectively, relative to the  
143 low-carbon endmember opal forming water. Though  $\delta^{13}\text{C}$  of the opal forming water cannot be directly  
144 measured, for the mixing curve to fit calcite compositions and opal  $\delta^{18}\text{O}$  values requires the opal forming  
145 endmember to be isotopically heavy ( $\delta^{13}\text{C} > -5$  ‰): a composition comparable to that of sub-AIS brines<sup>36,37</sup>.  
146 Similar mixing relationships are observed between the <sup>87</sup>Sr/<sup>86</sup>Sr and  $\delta^{18}\text{O}$  composition of opals and calcite

147 (Fig. 3c,d), requiring endmember waters to be distinct in both Sr concentration and isotopic composition.  
148 In both samples, the opal forming waters have more radiogenic (higher)  $^{87}\text{Sr}/^{86}\text{Sr}$  and heavier  $\delta^{18}\text{O}$  than the  
149 calcite forming waters. Sr:O mixing curves show that 20-fold and 50-fold of the total Sr in the system  
150 originates in the opal forming endmember (Fig. 3c, d). Due to their similar geochemical behavior, strontium  
151 and calcium concentrations in saline waters scale proportionally<sup>38</sup>. On this basis, the two endmember fluids  
152 must have distinctive Ca concentrations, with the opal forming endmember accounting for >95% of Ca in  
153 the system. This mixing relationship affirms the prevalence of two endmember waters with divergent  
154 concentrations: a highly Ca-rich opal forming brine that dominates the aqueous cation budget, and a  
155 relatively Ca-dilute, calcite forming meltwater that adds oxygen and carbon to the system.

156 Together, redox and isotopic data permit the identification of suitable analogs for both endmember  
157 waters. The opal endmember is characterized by low carbon and high calcium concentrations, an  $\delta^{13}\text{C}$   
158 enriched composition, a  $\delta^{18}\text{O}$  composition that matches ice proximal to the TAM, and a Ce\* value indicative  
159 of reducing fluids, supporting the idea that opal precipitated from a subglacial brine with limited access to  
160 oxygen. A potential analog for opal forming waters are  $\text{CaCl}_2$  brines that emanate from beneath the modern  
161 EAIS in the McMurdo Dry Valleys (MDV)<sup>39</sup>. In addition to the aforementioned similarities between the  
162 opal endmember and MDV brines, the REE (Extended Data Fig. 5) and  $\delta^{234}\text{U}_o$  (Table S1) of MDV  
163 brines<sup>40,41</sup> match opal compositions measured in our subglacial precipitates, and X-Ray fluorescence  
164 microprobe images show high abundance of  $\text{Cl}^-$  in opal layers (Extended Data Fig. 6). In comparison, the  
165 calcite endmember water has high carbon and low calcium concentrations, extremely depleted  $\delta^{13}\text{C}$  and  
166  $\delta^{18}\text{O}$  compositions, and a Ce\* signature indicative of oxidizing fluids. Combined, these geochemical  
167 signatures support a water composition analogous to glacial meltwater originating beneath the interior  
168 domes of East Antarctica, which would form from waters with highly depleted, oxygen-rich meltwater from  
169 dome-ice, can have high concentrations of depleted carbon from microbial respiration<sup>35,42</sup>, and would be  
170 much more dilute than marginal brines. Subglacial water measurements from the EAIS are few, but one  
171 candidate is C-rich, low salinity jökulhlaup water measured at Casey Station<sup>43</sup> that flush from subglacial  
172 lakes beneath Law Dome, and like the precipitates studied here, resulted in subglacial calcite precipitation  
173 during an AIM warm period<sup>44</sup>. Based on the highly depleted  $\delta^{18}\text{O}$  values and the mixing relationships  
174 between the two endmember fluids, we can rule out other possible endmember waters including  
175 hydrothermal fluids, which have been proposed as the source for calcite precipitates from Boggs Valley,  
176 East Antarctica<sup>45</sup>, but would result in reduced Ce\* signatures, heavier  $\delta^{18}\text{O}$  and  $\delta^{13}\text{C}$  values, and lower  
177  $\delta^{234}\text{U}_o$  values. Finally, while it is possible that the observed range of  $\delta^{18}\text{O}$  values between opal and calcite  
178 result from compositional variations in basal ice local to the precipitate locations, evidence from mixing  
179 relationships, redox variations, and the consistent geochemical differences between opal and calcite waters  
180 across 32 mineral transitions (Fig. 3; Extended Data Fig. 4) support the idea that the two minerals formed  
181 in distinct waters from the EAIS margin and interior respectively.

182 To test if endmember mixing is a plausible mechanism for the observed opal and calcite layers, we  
183 use the frezchem database<sup>39</sup> within the geochemical program PHREEQC<sup>46</sup> to simulate geochemical mixing  
184 of the two endmember waters identified in the above-mentioned analyses (see Methods for full description  
185 of PHREEQC models). Monomineralic opal layers represent periods of amorphous Si saturation, which  
186 can occur in subglacial environments through cryoconcentration<sup>47,48</sup>. Extended Data figure 7 shows a set of  
187 PHREEQC simulations that demonstrate opal saturation during freezing of a  $\text{CaCl}_2$  brine, while the  
188 deficiency of carbon in the brine precludes calcite precipitation. Since geochemical data suggest calcite  
189 precipitation from an oxidized, carbon-rich, and isotopically distinct glacial meltwater, we explore  
190 conditions under which calcite saturates upon mixing with plausible compositions of EAIS basal meltwater  
191 with  $\text{CaCl}_2$  brine. Mixing the Casey Station jökulhlaup water with opal-forming brines, we identify a strong  
192 supersaturation in calcite over a broad range of mixing proportions (Extended Data Fig. 8), and a cessation  
193 of opal precipitation consistent with discrete calcite pulses during mixing. This model predicts that calcite  
194 precipitation occurs immediately upon addition of meltwater to brine, while there could be a significant lag  
195 in opal precipitation as the aqueous system transitions back to basal freezing and cryoconcentration. Indeed,  
196 we may be seeing the effects of this lag in the temporal comparison between climate cycles and precipitate  
197 mineralogy, where nearly all warming events have a corresponding calcite layer (e.g., 180 and 190ka),

198 while some particularly short-lived cold events (<4kyr duration) do not have a detectable corresponding  
199 opal layer (e.g., 163 and 173 ka).

200

### 201 **Millennial-Scale Ice Sheet Thickness Changes Driven by Ocean Thermal Forcing**

202 The key finding from our subglacial precipitate archive is that millennial-scale ocean-atmosphere-  
203 cryosphere teleconnections cause a hydrologic response beneath the EAIS, where AIM warm phases drive  
204 enhanced delivery of subglacial meltwater from the interior to the ice sheet margin. Subsequent millennial  
205 cold phases then promote expansion of basal freezing causing the subglacial aqueous system near the ice  
206 sheet edge to become hydrologically isolated from the ice sheet interior. We investigate how millennial  
207 climate cycles may lead to shifts in subglacial hydrologic connectivity using a reduced complexity model  
208 of ice sheet thermodynamics, which simulates the evolution of basal melting and freezing rates in response  
209 to climate forcing (see supplementary text for full description). Our model framework assumes that ice  
210 thickness at the foothills of the TAM, which is by itself driven by the position of the grounding line in the  
211 Ross Embayment, is a linear function of the isotopic records of climate from either EDC (PRR50489) or  
212 WDC (MA113) ice cores (Fig. 1 b, f). Changing ice thickness feeds into variations in ice surface slope,  
213 basal shear stress, ice velocity, and basal shear heating, which affect the subglacial heat budget in the TAM.  
214 Calculated basal freezing/melting rates in the two inferred regions of sample formation provide a  
215 satisfactory match to the radiometrically dated records of calcite and opal precipitation from PRR50489  
216 and MA113 (Fig. 1c, i). This result is consistent with linear sensitivity of ice thickness in the Ross  
217 Embayment to the climatic variations reflected in isotopic ice core records from WAIS and EAIS, which  
218 are dominated by variability in ocean conditions with additional impacts of atmospheric temperature  
219 changes<sup>49</sup>. Scaling laws for ice sheet volumes<sup>50</sup> indicate a high sensitivity of ice volume to ice thickness  
220 changes, implying that the volume of AIS exhibited non-linear sensitivity to the millennial-scale climate  
221 forcing recorded in Antarctic ice cores. Collectively, our paired ice sheet thermodynamic simulations and  
222 precipitate record demonstrates that the ice on the EAIS side of the Ross Sea experiences significant  
223 thickness and volume fluctuations not only in response to large climate warming events during terminations,  
224 but also in response to climate cycles that are both smaller in amplitude and shorter in duration than major  
225 terminations, such as AIM events.

226 To produce basal freeze-melt cycles that are temporally correlated with precipitate opal-calcite  
227 transitions (Fig. 1c, i), our reduced complexity model of ice sheet thermodynamics requires changes to ice  
228 thickness on the order of hundreds of meters at the foothills of TAMs (e.g., near the mouth of the valley  
229 containing David Glacier for PRR50489) (Fig. S1, S2). Ice drawdown of a similar magnitude is observed  
230 in the Weddell Sea Embayment during post-LGM AIM events<sup>18,23</sup>, while models simulating AIS response  
231 to millennial-scale ocean-thermal forcing support the possibility of thickness change on this scale  
232 throughout the Pleistocene<sup>11</sup>. Our results imply that ice around the Ross Embayment exhibits a similarly  
233 high sensitivity to millennial-scale ocean thermal forcing during both glacial and interglacial background  
234 climate states. While our current dating uncertainties in AIS precipitates prevent us from determining  
235 whether ice response lags ocean forcing, the observed linear correlation between opal-calcite transitions  
236 and SH millennial climate cycles requires that ice thickness changes occurred at most, centuries after initial  
237 SO upwelling. Emerging models for the onset and duration of ice mass change in response to bipolar seesaw  
238 related climate cycles show similarly rapid ice loss events lasting centuries to millennial<sup>18</sup>.

239

### 240 **DISCUSSION**

241 The results presented here indicate that two chemical precipitates, separated by ~900km and  
242 deposited tens of thousands of years apart, form as a consequence of subglacial hydrologic cycles that match  
243 the patterns of SO and Antarctic climate changes recorded in ice cores, implying a link between AIS basal  
244 conditions and SH climate. More specifically, the site of precipitate formation oscillates between the  
245 freezing of local brines sourced from the proximity of the TAM during cold periods, and the influx of far  
246 field EAIS meltwaters during warm periods. Predictions of modern subglacial thermal conditions<sup>51,52</sup>  
247 indicate that large portions of the EAIS are at, or near the pressure melting point, with widespread melting  
248 in the ice sheet interior. In areas on the ice sheet periphery, thinner ice provides less insulation from cold

249 surface temperatures, resulting in basal freezing. Comparisons between simulations of modern basal melt  
250 rate<sup>52</sup> and precipitate collection sites (Fig. 2 b,c) show that both PRR50489 and MA113 are found within  
251 10 km of the boundary between basal freezing and melting predicted by an ice sheet model with 5-km  
252 horizontal resolution<sup>52</sup>. While the exact location of precipitate formation is unknown, several lines of  
253 evidence support their formation close to the collection site, and hence near the freeze-melt boundary.  
254 Specifically, dispersal of entrained sediment in basal ice follows a negative exponential decay law, making  
255 it far more likely for cobble-sized glacial sediments (PRR50489 and MA113 are 3 and 9cm thick) to  
256 originate within kilometers of the collection site rather than hundreds or thousands of kilometers<sup>53</sup>. The  
257 basal thermal regime also affects the likelihood of erosion and transport by the overlying ice, with the  
258 maximum degree of scouring and entrainment occurring in areas at the transition between basal melting  
259 upstream and basal freezing downstream<sup>54</sup>. Finally, both MA113 and PRR50489 are found in areas with  
260 very slow modern ice velocities<sup>25,55</sup>, which likely limits their transport distance to <50 km<sup>31</sup>. We therefore  
261 propose that the cycles of basal melting and freezing indicated by opal-calcite precipitates are the result of  
262 migrations of the basal thermal and hydrologic boundary, causing changes in the connectivity between  
263 waters from the interior and edge of the ice sheet following millennial-scale climate cycles (Extended Data  
264 Fig. 9).

265 Based on our reduced complexity model of ice sheet thermodynamics, the most parsimonious  
266 explanation for changes in subglacial hydrologic connectivity is periodic acceleration of ice flow. The  
267 driving mechanism for ice sheet acceleration on these timescales is generally regarded to be grounding line  
268 migration stemming from subsurface melting of ice shelves<sup>56</sup>. During millennial cold periods, grounded ice  
269 advances towards the continental shelf edge. As the bipolar seesaw takes effect, the ocean-atmosphere  
270 teleconnection between slowing AMOC and strengthening SH westerly winds drives upwelling of  
271 relatively warm circumpolar intermediate waters<sup>49</sup>, which contact ice shelves and grounding lines. Ice shelf  
272 thinning reduces back stress and increases ice discharge across the grounding lines<sup>5</sup>, leading to gradual  
273 catchment-scale ice flow acceleration<sup>9</sup>. Corresponding ice thinning starts near grounding lines and  
274 propagates upstream, leading to steepening of surface slopes and increased driving and basal shear stress.  
275 Higher ice flow rates and basal stress boost basal shear heating, which causes enhanced basal melting and  
276 increased subglacial hydrologic connectivity. Proxy records for SO sea surface temperature<sup>17</sup> and  
277 upwelling<sup>21</sup> provide evidence for millennial scale variations in-phase with the bipolar seesaw. Comparison  
278 between our subglacial precipitate record and SO sea surface temperature<sup>17</sup> shows a similar pattern of  
279 millennial-scale variability (Fig.1h), supporting bipolar seesaw-driven SO thermal forcing changes as a  
280 mechanism for millennial-scale AIS volume changes. This finding has implications for assessment of future  
281 mass loss from Antarctica triggered by ongoing anthropogenic warming and for interpretation of distal  
282 evidence for sea-level high stands during Quaternary warm climate periods<sup>57</sup>.

283 The basal thermal regime of AIS outlet glaciers is highly complex, with models demonstrating  
284 along-flow transitions between frozen and unfrozen basal conditions resulting from variations in bed  
285 topography, ice thickness, and flow rate along the ice sheet path<sup>58</sup>. While we acknowledge that localized  
286 basal temperature change could affect precipitate mineralogy, the collective geochronological and  
287 geochemical dataset presented here strongly favors hydrologic cycles driven by regional, rather than local,  
288 ice response. The consistent relationship between subglacial transitions from freezing to melting recorded  
289 at two different locations requires a highly regular triggering mechanism that is linked to the cryosphere  
290 and to the broader climate system. On both a glacier and regional scale, fluctuations between basal freezing  
291 and melting in the regions immediately upstream of our sample locations necessitate a change in ice sheet  
292 velocity or thickness, as atmospheric temperature change could not propagate to the ice sheet base on  
293 millennial timescales (see supplementary text for detailed explanation). This requisite dynamic ice sheet  
294 response implicates ocean forcing as the likely mechanism for the observed millennial-scale subglacial  
295 hydrologic changes regardless of spatial extent. Based on the locations of the two chemical precipitates  
296 studied here, an ocean-cryosphere teleconnection must operate in two catchments that are separated by  
297 ~900km and are not glaciologically linked, pointing to embayment-wide ice shelf mass fluctuation on  
298 millennial timescales. Geochemical evidence for millennial-scale flushing of dome-like meltwaters to  
299 marginal locations (Fig. 3) suggests that ice sheet acceleration in response to ice shelf perturbation enhances

300 hydrologic connectivity between subglacial waters separated by hundreds of kilometers. Given these  
301 spatiotemporal constraints, we conclude that opal-calcite transitions in subglacial precipitates result from  
302 millennial-scale migration of the regional freeze-melt boundary beneath grounded ice around the Ross  
303 Embayment.

304 Subglacial water has a significant effect on ice sheet motion, where ice sheet acceleration is often  
305 tied to the presence<sup>59</sup>, flushing<sup>60</sup>, and distribution<sup>61</sup> of subglacial water systems. Yet, the interaction between  
306 ice sheet dynamics and long-term changes in the subglacial hydrologic system in Antarctica are virtually  
307 unconstrained, largely due to the here-to-fore missing records documenting their long-term climate  
308 sensitivity. Here we have presented data from subglacial precipitates that provide evidence for millennial-  
309 scale acceleration of ice around the Ross Embayment, triggered by ocean thermal forcing. Our results show,  
310 for the first time, that the AIS responds to bipolar-seesaw related climate cycles regardless of the  
311 background climate state. Enhanced ice sheet velocity in the Ross Embayment causes hydrologic  
312 connectivity between the ice sheet interior and marginal regions. Added meltwater to previously frozen  
313 portions of the ice sheet can lubricate the bed and likely acts as feedback for further ice sheet acceleration  
314 and mass loss.

315

## 316 **METHODS**

### 317 **Subglacial precipitate opal-calcite timeseries**

318 Time series describing mineralogic shifts between opal and calcite in two subglacial precipitates are derived  
319 from <sup>234</sup>U-<sup>230</sup>Th ages combined with elemental characterization (see supplementary text for full <sup>234</sup>U-<sup>230</sup>Th  
320 dating methods). To construct the stratigraphic age model for each sample, we use a Bayesian Markov chain  
321 Monte Carlo model that considers the age of each layer and its stratigraphic position within the sample to  
322 refine the uncertainty of each date using a prior distribution based on the principle of superposition<sup>26</sup>.  
323 Elemental maps showing calcium and silicon concentration (Extended Data Fig. 2) were produced using  
324 Energy Dispersive X-ray Spectroscopy (EDS) measured on the ThermoScientific Apreo Scanning Electron  
325 Microscope (SEM) housed at UCSC. EDS data were generated using an Oxford Instruments UltimMax  
326 detector and were reduced using AZtecLive software. To quantify the opal-calcite transitions in the  
327 samples, Si and Ca concentration data were produced from line scans across precipitate layers (Extended  
328 Data Fig. 1). For sample MA113, detritus within two calcite layers results in Si peaks that do not correspond  
329 to opal. These areas are identified by high aluminium concentrations and are corrected to reflect a calcite  
330 composition. Timeseries in figure 1a and 1d were then generated by plotting the stratigraphic age model,  
331 against Ca concentration spectra. Within the error bounds of our precipitate age models and the ice core  
332 climate records, we are not able to estimate sub-millennial leads or lags between the AIS response and  
333 climate cycles. Nonetheless, stratigraphic consistency between dated layers, the regular frequency of mean  
334 ages, and the significant correlation between our mineralogic timeseries and climate proxy records supports  
335 our conclusion of a link between climate teleconnections and subglacial hydrology. Furthermore, as was  
336 previously mentioned, calcite layers form rapidly upon introduction of carbon-rich, alkaline waters from  
337 the EAIS interior to the marginal system, and the system then slowly transitions back to opal precipitation  
338 after hydrologic connectivity is shut off and the waters freeze. Therefore, it is possible that there is missing  
339 time between calcite layers that is not accounted for in stratigraphic age models. However, based on the  
340 regularity of opal depositional cycles, and the similarity between precipitate opal-calcite cycles and climate  
341 proxies, these unconformities do not represent enough time to disrupt the millennial-scale cyclicity of the  
342 precipitate mineralogy.

343 Correlation between opal-calcite timeseries from both samples and ice core climate records is  
344 assessed both visually, by plotting stacked spectra, and by moving window correlation coefficient<sup>62</sup>  
345 (Extended data Fig. 3). Although the link between subglacial hydrologic events and SH climate cycles is  
346 the result of a complex ocean-atmosphere-cryosphere feedback, stacked records reveal a clear overlap  
347 between the mineral transitions in precipitates and ice core climate proxies (Extended data Fig. 3a, c).  
348 Moving window Pearson r correlation coefficients show a significant linear correlation between precipitate  
349 and SH climate timeseries for both samples. The one exception to this synchrony is in sample MA113  
350 during the period between 54 and 50 ka. The lack of a clear relationship between the two records during

351 this timeframe could be the result of dating uncertainties in both MA113 and the ice core records, or poor  
352 millennial-scale climate resolution in the WDC during this period. Indeed, inspection of the TDC between  
353 54ka and 50ka shows small scale climate cycles that do not appear in WDC, and have a similar pattern to  
354 opal-calcite cycles in MA113 (Fig. 1d, e, f). Therefore, we find it likely that the three calcite peaks in  
355 MA113 correspond to the three small-scale warming events that appear in the TDC record.  
356

### 357 **Stable Isotopic Analyses**

358 Carbonate isotope ratios ( $\delta^{13}\text{C}_{\text{CO}_3}$  and  $\delta^{18}\text{O}_{\text{CO}_3}$ ) were measured by UCSC Stable Isotope Laboratory using a  
359 Thermo Scientific Kiel IV carbonate device and MAT 253 isotope ratio mass spectrometer. Referencing  
360  $\delta^{13}\text{C}_{\text{CO}_3}$  and  $\delta^{18}\text{O}_{\text{CO}_3}$  to VPDB is calculated by two-point correction to externally calibrated Carrara Marble  
361 'CM12' and carbonatite NBS-18<sup>63</sup>. Externally calibrated coral 'Atlantis II'<sup>64</sup> was measured for independent  
362 quality control. Typical reproducibility of replicates was significantly better than 0.05 ‰ for  $\delta^{13}\text{C}_{\text{CO}_3}$  and  
363 0.10 ‰ for  $\delta^{18}\text{O}_{\text{CO}_3}$ .

364 Opal layers were analyzed at the Stanford University Stable Isotope Biogeochemistry Laboratory  
365 for  $\delta^{18}\text{O}_{\text{SiO}_2}$  by conventional  $\text{BrF}_5$  fluorination (e.g. refs. <sup>65,66</sup>) and measured with  $\text{O}_2$  gas as the analyte on a  
366 Thermo Scientific MAT 253+ dual-inlet isotope ratio mass spectrometer (IRMS)<sup>67,68</sup>. Briefly, 2-3 mg opal  
367 samples were loaded into nickel reaction tubes as described in ref.<sup>69</sup> and heated for 2 hours at 250 °C at high  
368 vacuum. Samples were then repeatedly pre-fluorinated at room temperature with 30 mbar aliquots of  $\text{BrF}_5$   
369 until <1 mbar of non-condensable gas was present. A 30x stoichiometric excess of  $\text{BrF}_5$  was added to the  
370 nickel tubes and sealed. The nickel tubes were then heated at 600 °C for 16 hours to quantitatively produce  
371  $\text{O}_2$ . The generated  $\text{O}_2$  gas is then sequentially released into the cleanup line, cryogenically cleaned and  
372 frozen onto a 5Å mole sieve trap immersed in liquid nitrogen, equilibrated at room temperature with the  
373 IRMS dual-inlet sample-side bellows and measured for  $\delta^{18}\text{O}$  against a reference tank of known  $\delta^{18}\text{O}$   
374 composition (24.3‰) (for details refs. <sup>68,69</sup>). Opal  $\delta^{18}\text{O}$  is reported based on daily corrections made to four  
375 primary silicate standards (NBS-28, UWG-2, SCO and L1/UNM\_Q, which are quartz, garnet, olivine and  
376 quartz, respectively), spanning ~13‰, and have been recently calibrated to the VSMOW2-SLAP2 scale<sup>66,70</sup>.  
377 Three secondary standards (BX-88 (Stanford Laboratory internal standard), UCD-DFS (obtained from H.  
378 Spero, UC Davis; values reported in ref. <sup>71</sup>) and PS1772-8 (obtained from J. Dodd, Northern Illinois  
379 University; measured at U. of New Mexico and reported in ref. <sup>72</sup>, which are quartz, opal-CT and opal-A,  
380 respectively) were also analyzed over the course of the analyses. Replicate measurements of standards  
381 demonstrate reproducibility of <0.3‰ for all secondary and primary standards except the PS1772-8  
382 standard, though heterogeneity in this standard is suspected with laboratory averages reported in the  
383 literature<sup>72</sup> ranging from 40.2 to 43.6‰ (average value of 41.5‰ in this study).  
384

### 385 **Sr Isotopic Analyses**

386 Sr isotopic measurements were made at the UCSC Keck Isotope Laboratory. Sr compositions are measured  
387 on a TIMS in a one sequence static measurement: <sup>88</sup>Sr is measured on the Axial Faraday cup, while <sup>87</sup>Sr,  
388 <sup>86</sup>Sr, <sup>85</sup>Rb, and <sup>84</sup>Sr are measured on the low cups. Accuracy of the <sup>87</sup>Sr/<sup>86</sup>Sr measurements is evaluated  
389 using Sr standard SRM987 compared to a long-term laboratory average value of 0.71024, with a typical  
390 reproducibility of ±0.00004.  
391

### 392 **LA ICP-MS Methods**

393 Laser ablation inductively coupled plasma–mass spectrometry (LA ICP-MS) analyses were conducted at  
394 the Facility for Isotope Research and Student Training (FIRST) at Stony Brook University. Analyses were  
395 made using a 213 UV New Wave laser system coupled to an Agilent 7500cx quadrupole ICP-MS. The  
396 National Institute of Standards and Technology (NIST) 612 standard was used for approximate element  
397 concentrations using signal intensity ratios. Laser data were reduced in iolite<sup>73</sup>; element concentrations were  
398 processed with the trace-element data reduction schemes (DRS) in semiquantitative mode, which subtracts  
399 baselines and corrects for drift in signal.  
400

### 401 **Geochemical models of mineralogic cyclicity in subglacial precipitates:**

402 To understand the conditions under which discrete pulses of opal and calcite are precipitated following cold  
403 and warm Antarctic climate periods respectively, we integrate geochemical and isotopic characterization  
404 of the precipitates to inform simulations run using the aqueous geochemical modeling program  
405 PHREEQC<sup>46</sup>. The high ion concentrations of subglacial fluids necessitates the use of the Pitzer specific ion  
406 interaction approach, which allows PHREEQC to model the aqueous speciation and the mineral saturation  
407 index of brines, and has been shown to yield results<sup>39</sup> consistent with the subzero database FREZCHEM<sup>74</sup>.  
408 Our modeling approach to simulating opal-calcite transitions can be describe in three parts: 1) Identify the  
409 water composition and conditions under which opal will precipitate and calcite will not; 2) Identify the  
410 composition and volume of water required to mix with opal forming fluids to produce calcite; 3) Utilize the  
411  $\delta^{18}\text{O}$  and  $\delta^{13}\text{C}$  isotopic composition of calcite and opal, along with the known or inferred composition of  
412 mixing waters (Fig. 3) to constrain the relative volumes of brine and meltwater, thereby testing the validity  
413 of the mixing model. While the exact ionic strength of subglacial fluids and temperature of the subglacial  
414 aqueous system is unknown, we outline a plausible scenario for discrete layers of opal and calcite that fit  
415 modeled conditions at the base of the ice sheet<sup>51</sup>, and the geochemical constraints measured in precipitates.

416

#### 417 *PHREEQC Simulations Part 1*

418 Opal precipitation occurs when a solution is saturated with respect to amorphous silica. Opal solubility is  
419 both temperature and pH dependent<sup>75</sup>, with lower pH favoring precipitation. The silicon concentrations of  
420 subglacial waters<sup>76</sup> and mature brines that emanate from ice sheets<sup>77</sup> are typically tens of ppm, —values  
421 similar to other surface waters<sup>78</sup>— and Si concentration does not scale with total dissolved solids (TDS)<sup>79</sup>.  
422 At these relatively low Si concentrations, saturation of amorphous silica cannot be achieved without a  
423 mechanism to concentrate Si in solution. For aqueous systems beneath an ice sheet, this mechanism is very  
424 likely cryoconcentration via subglacial freezing, which extracts water from the cavity at the base of the ice  
425 sheet, concentrating solutes and raising mineral saturation<sup>48,80,81</sup>. Yet, most surface waters upon reaching  
426 saturation of amorphous silica will also be at saturation for calcite<sup>48,81</sup>, thus not matching the discrete opal  
427 layers observed in our precipitates. This suggests that the opals form from a mature brine<sup>79</sup> that is relatively  
428 free of  $\text{HCO}_3^-$ . A candidate fluid that fits these compositional criteria are  $\text{CaCl}_2$  brines, which occur in the  
429 McMurdo Dry Valleys (MDV) as shallow subsurface waters<sup>82–85</sup>, deep groundwaters<sup>39,84,86</sup>, and surface  
430 waters<sup>87–89</sup>, most notably feeding Lake Vanda<sup>77,90</sup> and Don Juan Pond (DJP)<sup>86,91,92</sup>. Ca-Cl-rich brines also  
431 occupy regions that were previously covered by the North American<sup>79</sup> and Fennoscandian ice sheet<sup>93</sup>,  
432 implying that they are a natural product of fluid isolation beneath ice sheets. Therefore,  $\text{CaCl}_2$  brines are a  
433 plausible composition for brine beneath the EAIS. The most geochemically well characterized MDV brines  
434 are those that feed DJP, therefore, we explore opal precipitation by equilibrating DJP brine with ice, calcite,  
435 and opal at a range of temperatures between  $-5^\circ\text{C}$  to  $5^\circ\text{C}$ . At full concentration, DJP brine causes melting  
436 of the overlying ice due to its exceptionally high ionic strength, resulting in significant dilution of the  
437 original solution, which inhibits opal precipitation (Extended Data Fig. 7a). Subsequent simulations of 10x  
438 and 50x diluted DJP brine over the same range of temperatures result in a gradual increase of opal saturation  
439 due to the incremental removal of water via cryoconcentration (Extended Data Fig. 7b, c). In these model  
440 runs, opal precipitation is controlled by the amount of water removed from the solution by freezing, which  
441 itself is controlled by ionic strength. At 10x concentrated, the solution does not freeze enough to drive opal  
442 precipitation, while opal is precipitated from the 50x diluted solution between  $-3^\circ\text{C}$  and  $-4^\circ\text{C}$ . A fourth  
443 PHREEQC model was run equilibrating DJP brine with ice, calcite, and opal over this temperature range,  
444 indicating that opal precipitation is reached once  $\sim 75\%$  of the water in the original solution is lost via  
445 freezing, which occurs at  $-3.5^\circ\text{C}$  (Extended Data Fig. 7d).

446

#### 447 *PHREEQC Simulations Part 2*

448 Simulation of calcite precipitation during AIM warm periods assumes that ‘meltwaters’ are mixed with the  
449 concentrated ‘glacial brines’ from part 1. The decision to model calcite precipitation using the admixture  
450 of new waters, rather than to reverse subglacial freezing, is based on the disparity in geochemistry between  
451 calcite and opal forming waters (Fig. 3; Extended Data Fig. 4). Based on the hypothesis that calcite layers  
452 form when waters from the EAIS interior are flushed to the ice sheet edge, meltwaters driving calcite

453 precipitation are likely to have become enriched in alkalinity and dissolved ions through water-rock  
454 interaction and chemical weathering of silicate minerals in the substrate during long-term storage beneath  
455 the EAIS. Calcite and opal data in  $^{87}\text{Sr}/^{86}\text{Sr}$  vs  $\delta^{18}\text{O}$  space provide further evidence that the two endmember  
456 waters —brine and subglacial meltwater— dissolve silicates with different provenance. Figure 3c and 3d  
457 show  $^{87}\text{Sr}/^{86}\text{Sr}$  vs  $\delta^{18}\text{O}$  mixing curve between opals and calcite, which indicate that the brine provides 98%  
458 of Sr to the system from a source with an  $^{87}\text{Sr}/^{86}\text{Sr}$  of 0.7135, while the meltwater endmember has a far  
459 lower concentration of Sr (2 %) derived from a reservoir with an  $^{87}\text{Sr}/^{86}\text{Sr}$  of 0.709. These data are consistent  
460 with a brine that weathers silicate minerals over long periods, and a meltwater that drives silicate weathering  
461 with a very different provenance over a relatively short time duration. The  $\delta^{13}\text{C}$  of the calcite (-23 ‰) (Fig.  
462 3, Extended Data Fig. 4) also provides evidence for the chemical composition of meltwaters, implying that  
463 they accumulated carbon through microbial respiration, which does not fractionate during the transition  
464 from aqueous  $\text{CO}_2$  to  $\text{HCO}_3^-$  if 100% of the carbon undergoes this conversion. Given, the similarity between  
465  $\delta^{13}\text{C}$  composition of calcite and that of respired carbon, it is unlikely that dissolution of sedimentary  
466 carbonates took place in the meltwater, which would have added a significantly less depleted source of  
467 carbon to the reservoir. This framework suggests that candidate compositions for calcite endmember fluids  
468 are waters with a similar history of subglacial exposure to glaciated sediments. The EAIS waters that best  
469 fit this description are jökulhlaup waters<sup>43</sup> observed near Casey Station, Antarctica. Using PHREEQC, we  
470 explore mixing of brine from part 1 with jökulhlaup waters from Casey Station<sup>43</sup>, by simulating a range of  
471 possible mixing ratios between brine and meltwater. We infer, based on the Ca:Sr ratios from other surface  
472 water systems that contain  $\text{CaCl}_2$  brine, that the ratio of Ca concentration between the brine and meltwater  
473 matches the ratio of Sr concentration between the two fluids (brine:meltwater = 98:2). Results show that  
474 without at least 30% meltwater the mixture too diluted with respect to Ca and  $\text{HCO}_3^-$  to precipitate calcite.  
475 PHREEQC mixing models successfully produced discrete pulses of calcite with mixtures between 30% and  
476 80% meltwater; conditions under which the admixture is undersaturated with respect to opal because the  
477 solution is too dilute with respect to Si and is supersaturated with respect to calcite leading to precipitation  
478 (Extended Data Fig. 8). Therefore, the addition of carbon-rich, alkaline meltwaters to opal precipitating,  
479 Ca-Cl-rich brines can trigger calcite supersaturation driving rapid calcite growth, consistent with our  
480 geochronologic outputs and calcite morphology. Collectively this modeling effort, along with the timescale  
481 data presented in figure 1, and the fibrous crystal textures, suggests that calcite forms rapidly after  
482 meltwaters are added to the subglacial aqueous system. However, the relative volume of meltwater added  
483 is unclear from these results alone and requires further isotopic constraints outlined below.

484

### 485 *C and O Isotopic Mixing Models Part 3*

486 For both the calcite and opal oxygen isotope data, the formation water  $\delta^{18}\text{O}$  (Fig. 3; Extended Data Fig. 4)  
487 is calculated using the appropriate equilibrium water-mineral fractionation factors assuming a temperature  
488 (T) of 0°C (273.15K). For calcite we use the empirical  $1000\ln\alpha$  versus  $1/T$  relationship of<sup>94</sup> and for opal the  
489  $1000\ln\alpha$  versus  $1/T^2$  relationship of<sup>95</sup> for T in kelvin. The  $1000\ln\alpha$  values for calcite and opal are 33.6‰  
490 and 44.2‰, respectively, and we calculate the formation waters avoiding the non-linearity associated with  
491 delta notation far from the standard of choice (in this case VSMOW). As such, we calculate the formation  
492 waters composition as:  $\alpha = (1000 + \delta^{18}\text{O}_{\text{mineral}}) / (1000 + \delta^{18}\text{O}_{\text{water}})$ .

493 Calcite data, in  $\delta^{13}\text{C}$  vs  $\delta^{18}\text{O}$  space, define a trend that suggests they form through admixture with  
494 an isotopically lighter water with respect to both carbon and oxygen. The carbon concentration dependent  
495 mixing curve that best fits that calcite data alone requires that the isotopically light endmember, what we'll  
496 refer to here as the “meltwater” endmember carries a higher DIC than the isotopically heavier water, which  
497 we'll now refer to as the brine endmember. In figure 3a and 3b, we assume that isotopically heaviest opals  
498 record the  $\delta^{18}\text{O}$  composition of the brine endmember and that the  $\delta^{13}\text{C}$  composition matches marine carbon  
499 derived from the substrate (-0 ‰), the latter of which is recorded by sodic carbonates suspected of forming  
500 from brines in the Lewis Cliff area<sup>96</sup>. Under such assumptions the carbon ratio between meltwater and brine  
501 is 97:3 for PRR50489 (Fig. 3a) and 80:20 in MA113 (Fig. 3b), a result that is consistent with the calcite  
502 precipitation model presented above, whereby the addition of a carbon rich, oxidized meltwater, to a  
503 reduced or intermediate  $\text{CaCl}_2$  brine, triggers calcite precipitation. As shown in extended data figure 8, the

504 calcite data imply formation when there is >30% of meltwater in the mixture. The array of calcite data can  
505 also be fit by a mixing model that assumes an isotopically lighter carbon composition ( $\delta^{13}\text{C} = -15\text{‰}$ ). While  
506 feasible, this is a less appealing solution, as a  $\delta^{13}\text{C}$  of  $-15\text{‰}$  does not match the composition of any specific  
507 carbon source and would require a mixture of waters. The data presented here suggests that over the  $\sim 100\text{ka}$   
508 of aggregate sample precipitation, there are two consistent endmember waters: a reduced brine that is locally  
509 derived (star in second quadrant, Fig. 3), and an oxidized meltwater that is from the polar plateau (star in  
510 third quadrant, Fig. 3).  
511

512 **References:**

- 513 1. Dutton, A. *et al.* Sea-level rise due to polar ice-sheet mass loss during past warm periods. *Science*  
514 (80- ). **349**, (2015).
- 515 2. Roberts, J. *et al.* Ocean forced variability of Totten Glacier mass loss. *Geol. Soc. Spec. Publ.* **461**,  
516 175–186 (2018).
- 517 3. Rintoul, S. R. *et al.* Ocean heat drives rapid basal melt of the totten ice shelf. *Sci. Adv.* **2**, 1–6  
518 (2016).
- 519 4. Joughin, I., Smith, B. E. & Medley, B. Marine ice sheet collapse potentially under way for the  
520 thwaites glacier basin, West Antarctica. *Science (80- )*. **344**, 735–738 (2014).
- 521 5. Joughin, I., Alley, R. B. & Holland, D. M. Ice-Sheet Response to Oceanic Forcing. *Science (80- )*.  
522 **338**, 1172–6 (2013).
- 523 6. Pollard, D. & DeConto, R. M. Modelling West Antarctic ice sheet growth and collapse through the  
524 past five million years. *Nature* **458**, 329–332 (2009).
- 525 7. DeConto, R. M. & Pollard, D. Contribution of Antarctica to past and future sea-level rise. *Nature*  
526 **531**, 591–597 (2016).
- 527 8. Mengel, M. & Levermann, A. Ice plug prevents irreversible discharge from east Antarctica. *Nat.*  
528 *Clim. Chang.* **4**, 451–455 (2014).
- 529 9. Reese, R., Gudmundsson, G. H., Levermann, A. & Winkelmann, R. The far reach of ice-shelf  
530 thinning in Antarctica. *Nat. Clim. Chang.* **8**, 53–57 (2018).
- 531 10. Golledge, N. R. *et al.* Antarctic contribution to meltwater pulse 1A from reduced Southern Ocean  
532 overturning. *Nat. Commun.* **5**, 1–8 (2014).
- 533 11. Blasco, J., Tabone, I., Alvarez-Solas, J., Robinson, A. & Montoya, M. The Antarctic Ice Sheet  
534 response to glacial millennial-scale variability. *Clim. Past* **15**, 121–133 (2019).
- 535 12. Crowley, T. J. North Atlantic Deep Water Cools the Southern Hemisphere. *Paleoceanography* **7**,  
536 489–497 (1992).
- 537 13. Pedro, J. B. *et al.* Beyond the bipolar seesaw: Toward a process understanding of interhemispheric  
538 coupling. *Quat. Sci. Rev.* **192**, 27–46 (2018).
- 539 14. Lu, J., Chen, G. & Frierson, D. M. W. The position of the midlatitude storm track and eddy-driven  
540 westerlies in aquaplanet AGCMs. *J. Atmos. Sci.* **67**, 3984–4000 (2010).
- 541 15. Schneider, T., Bischoff, T. & Haug, G. H. Migrations and dynamics of the intertropical  
542 convergence zone. *Nature* **513**, 45–53 (2014).
- 543 16. Marshall, J. & Speer, K. Closure of the meridional overturning circulation through Southern  
544 Ocean upwelling. *Nat. Geosci.* **5**, 171–180 (2012).
- 545 17. Anderson, H. J., Pedro, J. B., Bostock, H. C., Chase, Z. & Noble, T. L. Compiled Southern Ocean  
546 sea surface temperatures correlate with Antarctic Isotope Maxima. *Quat. Sci. Rev.* **255**, 106821  
547 (2021).
- 548 18. Weber, M. E., Golledge, N. R., Fogwill, C. J., Turney, C. S. M. & Thomas, Z. A. Decadal-scale  
549 onset and termination of Antarctic ice-mass loss during the last deglaciation. *Nat. Commun.* **12**,  
550 (2021).
- 551 19. Fretwell, P. *et al.* Bedmap2: Improved ice bed, surface and thickness datasets for Antarctica.  
552 *Cryosphere* **7**, 375–393 (2013).
- 553 20. Bohm, E. *et al.* Strong and deep Atlantic meridional overturning circulation during the last glacial  
554 cycle. *Nature* **517**, 73–76 (2015).
- 555 21. Ai, X. E. *et al.* Southern Ocean upwelling, Earth’s obliquity, and glacial-interglacial atmospheric  
556 CO<sub>2</sub> change. **1**, 1348–1352 (2020).
- 557 22. Weber, M. E. *et al.* Millennial-scale variability in Antarctic ice-sheet discharge during the last  
558 deglaciation. *Nature* **510**, 134–138 (2014).
- 559 23. Fogwill, C. J., Turney, C. S. M., Golledge, N. R., Etheridge, D. M. & Rubino, M. Antarctic ice  
560 sheet discharge driven by atmosphere-ocean feedbacks at the Last Glacial Termination. *Nature* 1–  
561 10 (2017). doi:10.1038/srep39979
- 562 24. Turney, C. S. M. *et al.* Early Last Interglacial ocean warming drove substantial ice mass loss from

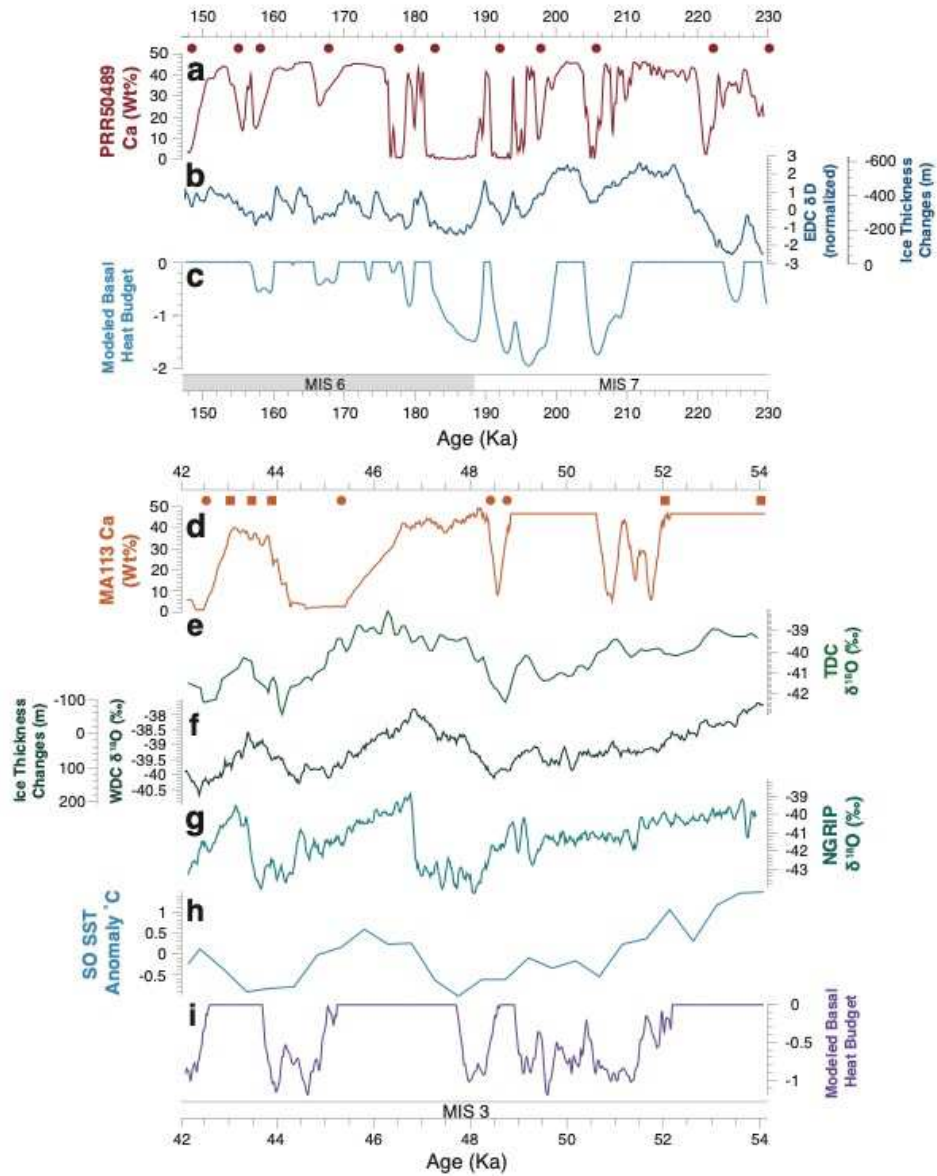
- 563 Antarctica. *Proc. Natl. Acad. Sci. U. S. A.* **117**, 3996–4006 (2020).
- 564 25. Kassab, C. M. *et al.* Formation and evolution of an extensive blue ice moraine in central  
565 Transantarctic Mountains, Antarctica. *J. Glaciol.* **66**, 49–60 (2019).
- 566 26. Keller, B. A Bayesian framework for integrated eruption age and age-depth modelling. (2020).  
567 doi:doi:10.17605/OSF.IO/TQX3F
- 568 27. Members, W. D. P. Precise inter-polar phasing of abrupt climate change during the last ice age.  
569 *Nature* **520**, 661–665 (2015).
- 570 28. Jouzel, J. *et al.* Orbital and millennial antarctic climate variability over the past 800,000 years.  
571 *Science (80-. )*. **317**, 793–796 (2007).
- 572 29. Andersen, K. K. *et al.* High-resolution record of Northern Hemisphere climate extending into the  
573 last interglacial period. *Nature* **431**, 147–151 (2004).
- 574 30. Aharon, P. Oxygen, carbon and U-series isotopes of aragonites from Vestfold Hills, Antarctica:  
575 Clues to geochemical processes in subglacial environments. *Geochim. Cosmochim. Acta* **52**, 2321–  
576 2331 (1988).
- 577 31. Graly, J. A., Licht, K. J., Kassab, C. M., Bird, B. W. & Kaplan, M. R. Warm-based basal sediment  
578 entrainment and far-field Pleistocene origin evidenced in central Transantarctic blue ice through  
579 stable isotopes and internal structures. *J. Glaciol.* **64**, 185–196 (2018).
- 580 32. Landais, A., Barkan, E. & Luz, B. Record of  $\delta^{18}\text{O}$  and  $^{17}\text{O}$ -excess in ice from Vostok Antarctica  
581 during the last 150,000 years. *Geophys. Res. Lett.* **35**, 1–5 (2008).
- 582 33. Masson-Delmotte, V. *et al.* A review of antarctic surface snow isotopic composition:  
583 Observations, atmospheric circulation, and isotopic modeling. *J. Clim.* **21**, 3359–3387 (2008).
- 584 34. German, C. R. & Elderfield, H. Application of the Ce anomaly as a paleoredox indicator: The  
585 ground rules. *Paleoceanography* **5**, 823–833 (1990).
- 586 35. Yan, Y. *et al.* Two-million-year-old snapshots of atmospheric gases from Antarctic ice. *Nature*  
587 **574**, (2019).
- 588 36. Murray, A. E. *et al.* Microbial life at  $-13^{\circ}\text{C}$  in the brine of an ice-sealed Antarctic lake. *Proc. Natl.*  
589 *Acad. Sci. U. S. A.* **109**, 20626–20631 (2012).
- 590 37. Doran, P. T., Kenig, F., Knoepfle, J. L., Mikucki, J. A. & Berry Lyons, W. Radiocarbon  
591 distribution and the effect of legacy in lakes of the McMurdo Dry Valleys, Antarctica. *Limnol.*  
592 *Oceanogr.* **59**, 811–826 (2014).
- 593 38. McNutt, R. H., Frappe, S. K., Fritz, P., Jones, M. G. & MacDonald, I. M. The  $^{87}\text{Sr}/^{86}\text{Sr}$  values of  
594 Canadian Shield brines and fracture minerals with applications to groundwater mixing, fracture  
595 history, and geochronology. *Geochim. Cosmochim. Acta* **54**, 205–215 (1990).
- 596 39. Toner, J. D. & Sletten, R. S. The formation of Ca-Cl-rich groundwaters in the Dry Valleys of  
597 Antarctica : Field measurements and modeling of reactive transport. *Geochim. Cosmochim. Acta*  
598 **110**, 84–105 (2013).
- 599 40. Lyons, W. B. *et al.* The Geochemistry of Englacial Brine From Taylor Glacier, Antarctica. *J.*  
600 *Geophys. Res. Biogeosciences* **124**, 633–648 (2019).
- 601 41. Lyons, W. B. *et al.* The carbon stable isotope biogeochemistry of streams, Taylor Valley,  
602 Antarctica. *Appl. Geochemistry* **32**, 26–36 (2013).
- 603 42. Christner, B. C. *et al.* A microbial ecosystem beneath the West Antarctic ice sheet. *Nature* **512**,  
604 310–313 (2014).
- 605 43. Goodwin, I. D. The nature and origin of a jokulhlaup near Casey Station, Antarctica. *J. Glaciol.*  
606 **34**, 95–101 (1988).
- 607 44. Goodwin, I. D. *et al.* Modern to Glacial age subglacial meltwater drainage at Law Dome, coastal  
608 East Antarctica from topography, sediments and jökulhlaup observations. *Geol. Soc. Spec. Publ.*  
609 **461**, 215–230 (2018).
- 610 45. Frisia, S. *et al.* The influence of Antarctic subglacial volcanism on the global iron cycle during the  
611 Last Glacial Maximum. *Nat. Commun.* **8**, 1–9 (2017).
- 612 46. Parkhurst, D. L. & Appelo, C. a. J. Description of Input and Examples for PHREEQC Version 3  
613 — A Computer Program for Speciation , Batch-Reaction , One-Dimensional Transport , and

- 614 Inverse Geochemical Calculations. U.S. Geological Survey Techniques and Methods, book 6,  
615 chapter A43, 497 p. *U.S. Geol. Surv. Tech. Methods, B. 6, chapter A43* 6-43A (2013).
- 616 47. Hallet, B. Deposits formed by subglacial precipitation of CaCO<sub>3</sub>. *Bull. Geol. Soc. Am.* **87**, 1003–  
617 1015 (1976).
- 618 48. Killawee, J. A., Fairchild, I. J., Tison, J. L., Janssens, L. & Lorrain, R. Segregation of solutes and  
619 gases in experimental freezing of dilute solutions: Implications for natural glacial systems.  
620 *Geochim. Cosmochim. Acta* **62**, 3637–3655 (1998).
- 621 49. Buizert, C. *et al.* Abrupt ice-age shifts in southern westerly winds and Antarctic climate forced  
622 from the north. *Nature* **563**, 681–684 (2018).
- 623 50. Bahr, D. B., Pfeffer, W. T. & Kasar, G. A review of volume-area scaling of glaciers. *Rev.*  
624 *Geophys.* **53**, 95–140 (2014).
- 625 51. Pattyn, F. Antarctic subglacial conditions inferred from a hybrid ice sheet / ice stream model.  
626 *Earth Planet. Sci. Lett.* **295**, 451–461 (2010).
- 627 52. Van Liefferinge, B. & Pattyn, F. Using ice-flow models to evaluate potential sites of million year-  
628 old ice in Antarctica. *Clim. Past* **9**, 2335–2345 (2013).
- 629 53. Clark, P. U. Subglacial Sediment Dispersal and till Composition. *J. Geol.* **95**, 527–541 (1987).
- 630 54. Sugden, D. E. Glacial Erosion by the Laurentide Ice Sheet. *J. Glaciol.* **20**, 367–391 (1978).
- 631 55. Coren, F., Delisle, G. & Sterzai, P. Ice dynamics of the Allan Hills meteorite concentration sites  
632 revealed by satellite aperture radar interferometry. *Meteorit. Planet. Sci.* **38**, 1319–1330 (2003).
- 633 56. Schoof, C. Ice sheet grounding line dynamics: Steady states, stability, and hysteresis. *J. Geophys.*  
634 *Res. Earth Surf.* **112**, 1–19 (2007).
- 635 57. Grant, K. M. *et al.* Sea-level variability over five glacial cycles. *Nat. Commun.* **5**, (2014).
- 636 58. Gollledge, N. R., Marsh, O. J., Rack, W., Braaten, D. & Jones, R. S. Basal conditions of two  
637 Transantarctic Mountains outlet glaciers from observation-constrained diagnostic modelling. *J.*  
638 *Glaciol.* **60**, 855–866 (2014).
- 639 59. Bell, R. E., Studinger, M., Shuman, C. A., Fahnestock, M. A. & Joughin, I. Large subglacial lakes  
640 in East Antarctica at the onset of fast-flowing ice streams. *Nature* **445**, 904–907 (2007).
- 641 60. Stearns, L. A., Smith, B. E. & Hamilton, G. S. Increased flow speed on a large east antarctic outlet  
642 glacier caused by subglacial floods. *Nat. Geosci.* **1**, 827–831 (2008).
- 643 61. Creyts, T. T. & Schoof, C. G. Drainage through subglacial water sheets. *J. Geophys. Res. Earth*  
644 *Surf.* **114**, 1–18 (2009).
- 645 62. Mack, D. J. movcorr(x, y, k, varargin): Compute windowed correlation coefficient. (2022).
- 646 63. Coplen, T. B. *et al.* New Guidelines for  $\delta^{13}\text{C}$  Measurements. *Anal. Chem.* **78**, 2439–2441 (2006).
- 647 64. Ostermann, D. R. & Curry, W. B. Calibration of stable isotopic data: An enriched  $\delta^{18}\text{O}$  standard  
648 used for source gas mixing detection and correction. *Paleoceanography* **15**, 353–360 (2000).
- 649 65. Clayton, R. N. & Mayeda, T. K. The use of bromine pentafluoride in the extraction of oxygen  
650 from oxides and silicates for isotopic analysis. *Geochim. Cosmochim. Acta* **27**, 43–52 (1963).
- 651 66. Wostbrock, J. A. G. *et al.* Calibration and application of silica-water triple oxygen isotope  
652 thermometry to geothermal systems in Iceland and Chile. *Geochim. Cosmochim. Acta* **234**, 84–97  
653 (2018).
- 654 67. Chamberlain, C. P. *et al.* Triple oxygen isotopes of meteoric hydrothermal systems - implications  
655 for palaeoaltimetry. *Geochemical Perspect. Lett.* **15**, 6–9 (2020).
- 656 68. Ibarra, D. E., Kukla, T., Methner, K. A., Mulch, A. & Chamberlain, C. P. Reconstructing Past  
657 Elevations From Triple Oxygen Isotopes of Lacustrine Chert: Application to the Eocene  
658 Nevadaplano, Elko Basin, Nevada, United States. *Front. Earth Sci.* **9**, 1–19 (2021).
- 659 69. Ibarra, D. E. *et al.* Triple oxygen isotope systematics of diagenetic recrystallization of diatom  
660 opal-A to opal-CT to microquartz in deep sea sediments. *Geochim. Cosmochim. Acta* (2021).  
661 doi:10.1016/j.gca.2021.11.027
- 662 70. Sharp, Z. D. & Wostbrock, J. A. G. Standardization for the Triple Oxygen Isotope System:  
663 Waters, Silicates, Carbonates, Air, and Sulfates. *Rev. Mineral. Geochemistry* **86**, 179–196 (2021).
- 664 71. Menicucci, A. J., Matthews, J. A. & Spero, H. J. Oxygen isotope analyses of biogenic opal and

- 665 quartz using a novel microfluorination technique. *Rapid Commun. Mass Spectrom.* **27**, 1873–1881  
666 (2013).
- 667 72. Chaplign, B. *et al.* Inter-laboratory comparison of oxygen isotope compositions from biogenic  
668 silica. *Geochim. Cosmochim. Acta* **75**, 7242–7256 (2011).
- 669 73. Paton, C., Hellstrom, J., Paul, B., Woodhead, J. & Hergtb, J. Iolite : Freeware for the visualisation  
670 and processing of mass spectrometric data. *J. Anal. At. Spectrom.* **26**, 2508–2518 (2011).
- 671 74. Marion, G. M., Mironenko, M. V. & Roberts, M. W. FREZCHEM: A geochemical model for cold  
672 aqueous solutions. *Comput. Geosci.* **36**, 10–15 (2010).
- 673 75. Iler, R. K. *The Chemistry of Silica: Solubility, Polymerization, Colloid and Surface Properties,*  
674 *and Biochemistry.* John Wiley and Sons Ltd., New York. (1979).
- 675 76. Hawkings, J. R. *et al.* Enhanced trace element mobilization by Earth’s ice sheets. *Proc. Natl.*  
676 *Acad. Sci.* 1–12 (2020). doi:10.1073/pnas.2014378117
- 677 77. Green, W. J. & Canfield, D. E. Geochemistry of the Onyx River (Wright Valley, Antarctica) and  
678 its role in the chemical evolution of Lake Vanda. *Geochim. Cosmochim. Acta* **48**, 2457–2467  
679 (1984).
- 680 78. Tréguer, P. *et al.* The silica balance in the world ocean: A reestimate. *Science (80-. )*. **268**, 375–  
681 379 (1995).
- 682 79. Frapé, S. K., Fritz, P. & McNutt, R. H. Water-rock interaction and chemistry of groundwaters  
683 from the Canadian Shield. *Geochim. Cosmochim. Acta* **48**, 1617–1627 (1984).
- 684 80. Bell, R. E. *et al.* Widespread Persistent Thickening of the East Antarctic Ice Sheet by Freezing  
685 from the Base. *Science (80-. )*. **331**, 1592–1596 (2011).
- 686 81. Hallet, B. Deposits Formed by Subglacial Precipitation of CaCO<sub>3</sub>. *Geol. Soc. Am. Bull.* **87**, 1003–  
687 1015 (1976).
- 688 82. Wilson, A. T. Geochemical problems of the Antarctic dry areas. *Nature* **280**, 205–208 (1979).
- 689 83. Webster, J. G., Goguel, R. L. & Pond, D. J. Anions and alkali metals in Lake Vanda , Don Juan  
690 Pond , and the Onyx River : Further indications of brine origin. 154–156 (1988).
- 691 84. Cartwright, K. & Harris, H. J. H. Hydrogeology of the Dry Valley region, Antarctica. *Am.*  
692 *Geophys. Union, Antarct. Res. Ser.* **33**, 193–214 (1981).
- 693 85. Levy, J. S., Fountain, A. G., Welch, K. A. & Lyons, W. B. Hypersaline ‘wet patches’ in Taylor  
694 Valley, Antarctica. *Geophys. Res. Lett.* **39**, 1–5 (2012).
- 695 86. Harris, H. J. H. & Cartwright, K. Hydrology of the Don Juan Basin, Wright Valley, Antarctica.  
696 *Antarct. Res. Ser.* **33**, 162–184 (1981).
- 697 87. Angino, E. E. & Armitage, K. B. A Geochemical Study of Lakes Bonney and Vanda, Victoria  
698 Land, Antarctica. *J. Geol.* **71**, 89–95 (1963).
- 699 88. Healy, M., Webster-Brown, J. G., Brown, K. L. & Lane, V. Chemistry and stratification of  
700 Antarctic meltwater ponds II: Inland ponds in the McMurdo Dry Valleys, Victoria Land. *Antarct.*  
701 *Sci.* **18**, 525–533 (2006).
- 702 89. Lyons, W. B. *et al.* The geochemistry of upland ponds, Taylor Valley, Antarctica. *Antarct. Sci.* **24**,  
703 3–14 (2012).
- 704 90. Carlson, C. A., Phillips, F. M., Elmore, D. & Bentley, H. W. Chlorine-36 tracing of salinity  
705 sources in the Dry Valleys of Victoria Land, Antarctica. *Geochim. Cosmochim. Acta* **54**, 311–318  
706 (1990).
- 707 91. Dickson, J. L., Head, J. W., Levy, J. S. & Marchant, D. R. Don Juan Pond, Antarctica: Near-  
708 surface CaCl<sub>2</sub>-brine feeding Earth’s most saline lake and implications for Mars. *Sci. Rep.* **3**, 1–8  
709 (2013).
- 710 92. Toner, J. D., Catling, D. C. & Sletten, R. S. The geochemistry of Don Juan Pond: Evidence for a  
711 deep groundwater flow system in Wright Valley, Antarctica. *Earth Planet. Sci. Lett.* **474**, 190–197  
712 (2017).
- 713 93. Nurmi, P. A., Kukkonen, I. T. & Lahermo, P. W. Geochemistry and origin of saline groundwaters  
714 in the Fennoscandian Shield. *Appl. Geochemistry* **3**, 185–203 (1988).
- 715 94. Kim, S. T. & O’Neil, J. R. Equilibrium and nonequilibrium oxygen isotope effects in synthetic

716 carbonates. *Geochim. Cosmochim. Acta* **61**, 3461–3475 (1997).  
717 95. Sharp, Z. D. *et al.* A calibration of the triple oxygen isotope fractionation in the SiO<sub>2</sub>-H<sub>2</sub>O system  
718 and applications to natural samples. *Geochim. Cosmochim. Acta* **186**, 105–119 (2016).  
719 96. Fitzpatrick, J. J., Muhs, D. R. & Jull, A. J. T. Saline Minerals in the Lewis Cliff Ice Tongue,  
720 Buckley Island Quadrangle, Antarctica. *Contrib. to Antarct. Res. I* **50**, 57–69 (1990).  
721 97. Veres, D. *et al.* The Antarctic ice core chronology (AICC2012): An optimized multi-parameter  
722 and multi-site dating approach for the last 120 thousand years. *Clim. Past* **9**, 1733–1748 (2013).  
723 98. Steig, E. J. *et al.* Wisconsinan and Holocene climate history from an ice core at Taylor Dome,  
724 western Ross embayment, Antarctica. *Geogr. Ann. Ser. A Phys. Geogr.* **82**, 213–235 (2000).  
725 99. Grootes, P. M. *et al.* The Taylor Dome Antarctic 18O record and globally synchronous changes in  
726 climate. *Quat. Res.* **56**, 289–298 (2001).  
727 100. Phillips, D. L. & Koch, P. L. Incorporating concentration dependence in stable isotope mixing  
728 models. *Oecologia* **130**, 114–125 (2002).  
729  
730  
731  
732  
733  
734  
735  
736  
737  
738  
739  
740  
741  
742  
743  
744  
745  
746  
747  
748  
749  
750  
751  
752  
753  
754  
755  
756  
757  
758  
759  
760  
761  
762  
763  
764  
765  
766

767  
 768  
 769  
 770  
 771  
 772  
 773  
 774  
 775  
 776  
 777  
 778  
 779  
 780  
 781  
 782  
 783  
 784  
 785  
 786  
 787  
 788  
 789  
 790  
 791  
 792  
 793  
 794  
 795  
 796  
 797  
 798  
 799  
 800  
 801  
 802  
 803  
 804  
 805  
 806  
 807  
 808  
 809  
 810



811 **Fig. 1 | Comparison of precipitate mineralogy with climate records.** **a.** Subglacial precipitate sample  
 812 PRR50489 Ca concentration. **b.**  $\delta D$  measured in EPICA Dome C Ice Core (EDC)<sup>28,97</sup>. EDC record is  
 813 detrended and converted to a z-score by zero-mean normalization to eliminate orbital trends. **c.** Reduced  
 814 complexity model output of basal heat budget over the time frame of sample PRR50489 in units of mm/year  
 815 of equivalent basal freezing rate. Negative values indicate freezing. Positive values correspond to basal  
 816 melting and are truncated at 0 mm/yr because we consider any positive values to be sufficient to maintain  
 817 hydrologic connectivity to regional subglacial waters. **d.** Subglacial precipitate sample MA113 Ca

818 concentration. **e.**  $\delta^{18}\text{O}$  measured in Taylor Dome Ice Core (TDC)<sup>98,99</sup> **f.**  $\delta^{18}\text{O}$  measured in West Antarctic  
819 Divide Ice Core (WDC)<sup>27</sup>. **g.**  $\delta^{18}\text{O}$  measured in Northern Greenland Ice Core Project (NGRIP)<sup>29</sup>. **h.**  
820 Southern Ocean sea surface temperature anomalies from stacked drill core records<sup>17</sup>. **f.** as in **c.** for sample  
821 MA113. Positive values correspond to basal melt and are truncated at 0 mm/year. High values in precipitate  
822 records represent calcite precipitation; low values represent opal precipitation. Markers above **a** and **d** show  
823 the location of dated layers; square markers represent calcite ages; circles represent opal ages. Records in  
824 **b**, **g**, and **h** are synchronized to AICC2012 chronology; the record in **f** is synchronized WD2014 chronology,  
825 the record in **e** is visually tuned to match the record in **f**. Isotope ratios are on the VSMOW (Vienna Standard  
826 Mean Ocean Water) scale. Marine Isotope substages are marked in grey and white and are labeled. Forcing  
827 for reduced complexity model of ice thermodynamics is provided by ice thickness changes at the Foothills  
828 of the TAM, which are parameterized as a linear function of the ice core isotopic record. The magnitude  
829 and scale of these thickness changes is shown on the right y-axis of **b**. and **f**.  
830

831  
832  
833  
834  
835  
836  
837  
838  
839  
840  
841  
842  
843  
844  
845  
846  
847  
848  
849  
850  
851  
852  
853  
854  
855  
856  
857  
858  
859  
860  
861  
862  
863  
864  
865  
866  
867  
868  
869  
870  
871  
872  
873  
874  
875  
876  
877  
878  
879  
880  
881

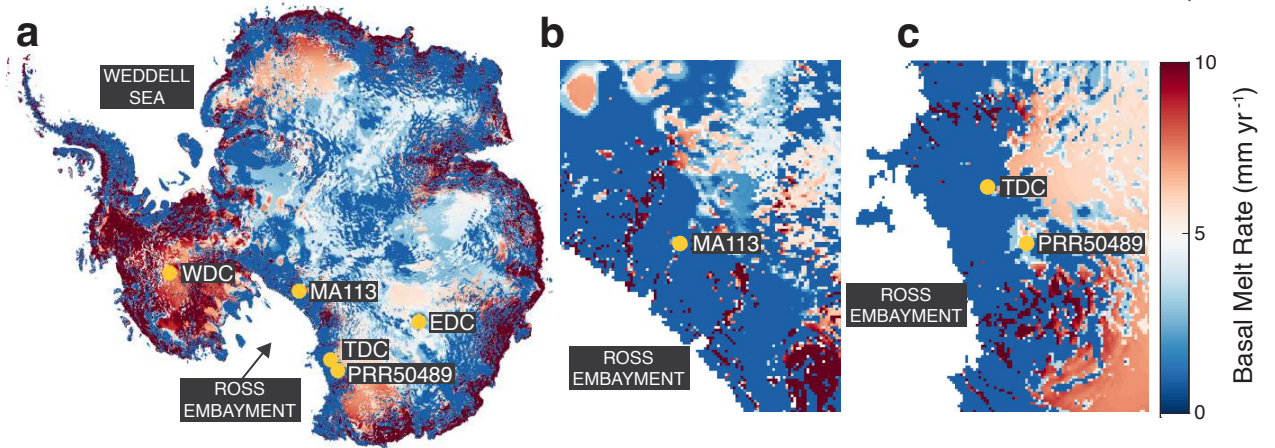


**Fig. 2 | Antarctic Mean Basal Melt Rate.** **a.** Map of estimated modern mean basal melt rate<sup>52</sup> truncated at 10mm yr<sup>-1</sup>. Dark blue areas are frozen at the bed, white to red areas experience basal melting. **b.** Map zoomed in to show basal melt rate near location of MA113. **c.** Map zoomed in to show basal melt rate near location of PRR50489. Markers indicate locations of spectra shown in figure 2.

882  
 883  
 884  
 885  
 886  
 887  
 888  
 889  
 890  
 891  
 892  
 893  
 894  
 895  
 896  
 897  
 898  
 899  
 900  
 901  
 902  
 903  
 904  
 905  
 906  
 907  
 908  
 909  
 910  
 911  
 912  
 913  
 914  
 915  
 916  
 917  
 918  
 919  
 920  
 921  
 922  
 923  
 924  
 925  
 926

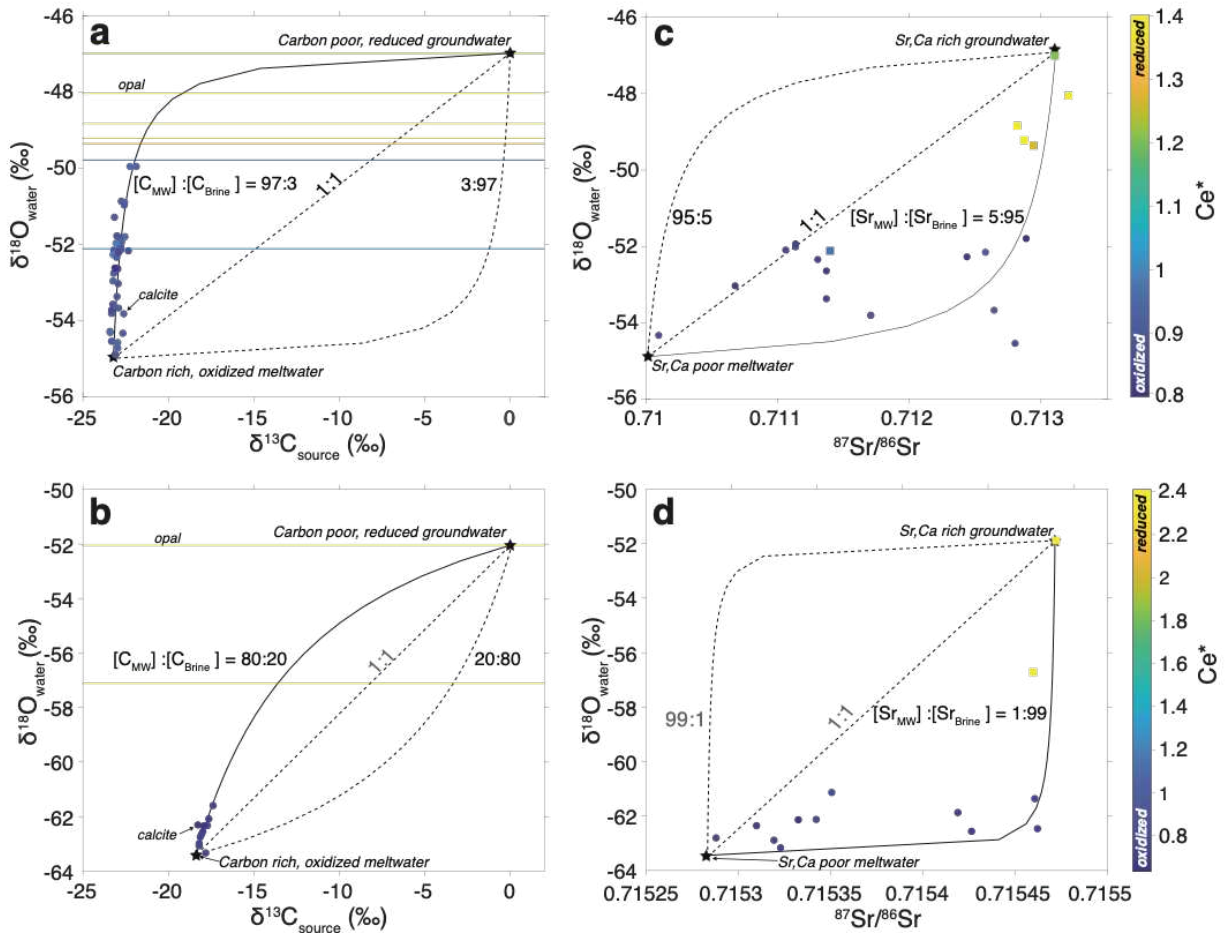


**Fig. 3 | Stable isotope mixing models for precipitates PRR50489 and MA113.** **a.**  $\delta^{18}\text{O}$  of the precipitating fluid versus  $\delta^{13}\text{C}$  composition of the C source, plotted for PRR50489 calcite (markers) and opal (horizontal lines). Endmembers (stars) include an opal precipitating fluid that is a carbon poor, reduced brine; and a calcite precipitating fluid that is a carbon rich, oxidizing meltwater. Solid curved line represents mixing model between the two endmembers<sup>100</sup>. To fit calcite data, mixing model requires meltwater to have a total carbon concentration 40-fold higher than brine. **b.** As in **a**, but data are from sample MA113. To fit calcite data, mixing model requires meltwater to have a total carbon concentration 5-fold higher than brine. **c.**  $\delta^{18}\text{O}$  of the precipitating fluid versus  $^{87}\text{Sr}/^{86}\text{Sr}$  composition of the Sr source, plotted for PRR50489 calcite (circles) and opal (squares). To fit data, mixing model requires meltwater to have a total strontium concentration 20-fold higher than brine. **d.** As is **c**, but data are from MA113. To fit data, mixing model requires meltwater to have a total strontium concentration 50-fold higher than brine. Dashed lines represent mixing models with different C or Sr ratios. All data are color coded by  $\text{Ce}^*$  value, with blue being the lowest, most oxidizing values, and yellow being the highest, most reducing values. Oxygen isotopic compositions corrected to water compositions assuming equilibrium fractionation during calcite formation and a formation of  $0^\circ\text{C}$ .

## Supplementary Files

This is a list of supplementary files associated with this preprint. Click to download.

- [ExtendedDataTable3.xlsx](#)
- [ExtendedDataFigures.pdf](#)
- [ExtendedDataTable4.xlsx](#)
- [ExtendedDataTable2.xlsx](#)
- [ExtendedDataTable1.xlsx](#)
- [SupplementaryText.pdf](#)